energies

MDPI

Article

Reservoir Characteristics of the Lower Jurassic Lacustrine Shale in the Eastern Sichuan Basin and Its Effect on Gas Properties: An Integrated Approach

Jianhua He [1,2,*], Hucheng Deng [2,*], Ruolong Ma [2], Ruyue Wang [3], Yuanyuan Wang [2] and Ang Li [4]

1 State Key Laboratory of Shale Oil and Gas Enrichment Mechanisms and Effective Development, Beijing 100083, China
2 College of Energy, Chengdu University of Technology, Chengdu 610059, China; lugang19@cdut.edu.cn (R.M.); wangyuanyuan1919@outlook.com (Y.W.)
3 Petroleum Exploration and Production Research Institute, China Petroleum and Chemical Corporation, Beijing 100083, China; wangruyue.syky@sinopec.com
4 Wuxi Research Institute of Petroleum Geology, Sinopec Petroleum & Production Research Institute, Wuxi 214000, China; syky@sinopec.com
* Correspondence: hejianhuadizhi@163.com (J.H.); denghucheng@cdut.cn (H.D.)

Received: 14 July 2020; Accepted: 25 August 2020; Published: 31 August 2020

Abstract: The exploration of shale gas in Fuling area achieved great success, but the reservoir characteristics and gas content of the lower Jurassic lacustrine in the northern Fuling areas remain unknown. We conducted organic geochemical analyses, Field Emission Scanning Electron Microscope (FE-SEM), X-ray diffraction (XRD) analysis, high-pressure mercury intrusion (MIP) and CH_4adsorption experimental methods, as well as NMR logging, to study mineral composition, geochemical, pore structure characteristics of organic-rich shales and their effects on the methane adsorption capacity. The Da'anzhai shale member is generally a set of relatively thick (avg. 75 m) and high carbonate-content (avg. 56.89%) lacustrine sediments with moderate total organic carbon (TOC) (avg. 1.12%) and thermal maturation (Vitrinite reflectance (VR): avg. 1.19%). Five types of lithofacies can be classified: marl (ML), calcareous shale (CS), argillaceous shale (AS), muddy siltstone (MS), and silty shale (SS). CS has good reservoir quality with a high porosity (avg. 4.72%). The small pores with the transverse relaxation time of 0.6–1 ms and 1–3 ms comprised the major part of the porosity in the most lithofacies from Nuclear magnetic resonance (NMR) data, while the large pore (>300 ms) accounts for a small porosity proportion in the CS. The pores mainly constitute of mesopores (avg. 23.2 nm). The clay minerals with a large number of interparticle pores in the SEM contributes most to surface area in the shale lithofacies with a moderate TOC. The adsorption potential of shale samples is huge with an average adsorption capacity of 4.38 mL/g and also has high gas content (avg. 1.04 m^3/t). The adsorption capacity of shale samples increases when TOC increases and temperature decreases. Considered reservoir properties and gas properties, CS with the laminated structures in the medium-upper section of the Da'anzhai member is the most advantage lithofacies for shale gas exploitation.

Keywords: shale gas; reservoir characteristics; gas content; eastern Sichuan Basin; the Da'anzhai member

1. Introduction

A great success of shale gas exploration has been made in a Fuling gas field. Recently, many more oil and gas discoveries in lacustrine shale of the Lower Jurassic succession (e.g., Da'anzhai member shale) in the northern Fuling area gives a rise to the possibility of nonmarine shale gas accumulation in neighboring areas [1,2]. Recent studies focus on the pore structure and geochemical characteristics

of the Da'anzhai member lacustrine shale [3–5]. There is little research concerning the influence of lacustrine shale reservoir characteristics on the adsorption capacity and total gas content. However, gas content is not only a key factor of favorable shale gas area evaluation, but also controls whether shale reservoir has a commercial exploration value or not [2,6].

In this study, we present a comprehensive approach of mineral composition and geochemical tests, high-resolution imaging investigation, high-pressure mercury intrusion (MIP) and CH_4adsorption experiments, as well as NMR well logging, to (1) determine the mineral composition and geochemical, pore structure and petrophysical characteristics of the different shale lithofacies in the Da'anzhai members; (2) study the influence of continental reservoir characteristics on shale gas properties; (3) optimize the advantageous shale lithofacies to provide guidance for selecting the target shale gas layers.

2. Geological Setting

The study area is located in the eastern part of the Sichuan Basin, which is one of the major petroliferous basins in China. This area is dominated by the huge thrust-fold belts with an NNE or NE striking. It includes the narrow Datianchi, Huangnitang, Dachigan, Fangdoushan anticlines and gentle Liangping, Bashansi synclines between these structures from east to west [7]. The North Fuling gas field is located in the Bashansi Synclines (Figure 1A,B). The Ziliujing formation in the Lower Jurassic is divided into Da'anzhai, Maanzhan, and Dongyuemiao members. The target layer of theDa'anzhai member consists of three lithological members: the shell limestone in the lower layer (J_1zDa^1); the interbed in the middle layer with black shale, silty shale, and shell limestone (J_1zDa^2); and the shell limestone and marl in the top (J_1zDa^3) (Figure 1C). The middle part of the Da'anzhai member (J_1zDa^2) is the most important source rock with a thickness of 30–80 m. This layer was widely deposited when the lacustrine system was rapidly expanded and the water within the lake was deepened [8], which produced a positive impact on the accumulation and preservation of organic matter.

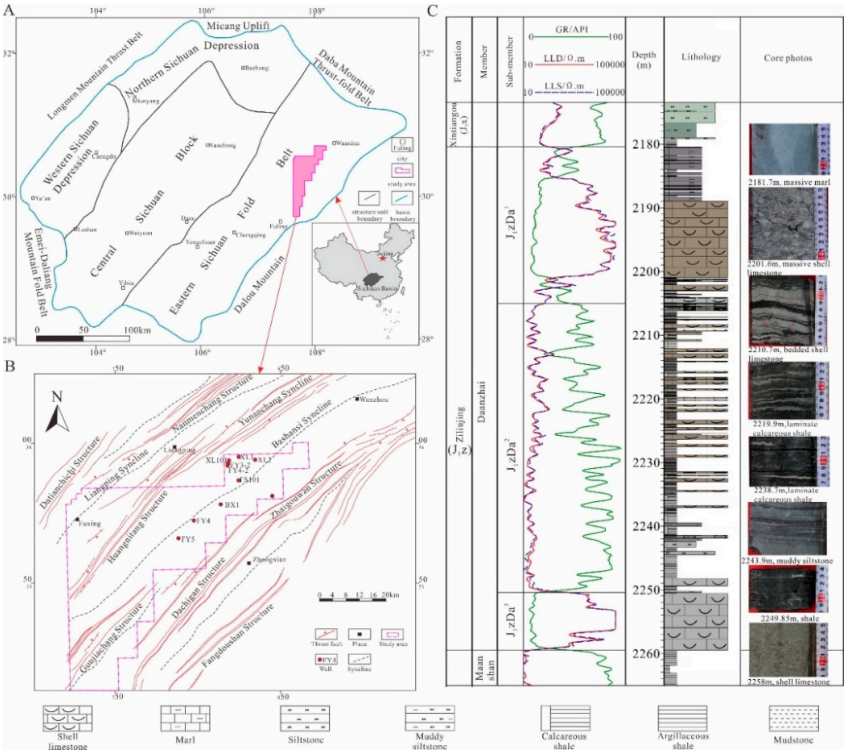

Figure 1. Study location (**A**), geological map (**B**), and simplified stratigraphic column (**C**) of the Jurassic Da'anzhai member in the Eastern Sichuan Basin.

3. Samples and Experiments

In this paper, all the samples in the Da'anzhai member were selected from fresh cores in five wells, including FY1, FY4, FY5, FY3-2, and XL101 wells. Most of the samples were analyzed in the following methods: Total organic carbon determination, Rock-Eval pyrolysis analyses, kerogen vitrinite reflectance analysis, kerogen maceral composition microscopy, X-ray diffraction (XRD) testing, and high-pressure mercury intrusion (MIP), that were performed by the Marine Geology Lab, PetroChina Jianghan Oilfield Company. High-pressure intrusion experiments were conducted by AutoPore IV 9520 instruments, which can obtain a pore size range of 0.003–1000 μm. The pore micromorphology of 15 samples were determined at the State Key Laboratory of Oil and Gas Reservoir Geology and Exploitation of Chengdu University of Technology. These samples were investigated using an "FEI Quanta model 200F from FEI corporation, Netherlands" field-emission scanning electron microscopy (FE-SEM) under a working condition of 20 kv and distance of 8–9 mm. The methane adsorption isotherm experiments of five samples were conducted by the Shale Gas Lab, Sichuan Coal Geology Bureau.

Nuclear magnetic resonance (NMR) well logging is an approach that confirms the nuclear spin states of hydrogen in water and oil within a thin annulus situated deeply into the formation with several inches [9]. Under the pulsed and static magnetic field, the transverse relaxation time (T_2) of protons generally shows a positive relationship with the amount of hydrogen protons in the pore fluid [10]. The NMR well logging curves generally shows 2 to 3 main peaks and the peaks becomes larger with higher relaxation time: the first peak in the shale reservoir normally is the predominant one indicating clay-bound water and capillary-bound water, while free-fluid volume and micro-fractures are only revealed in some small peaks [11].

Field desorption is a relatively accurate method to directly obtain the data of gas content, including desorption gas content, losing gas content and residual gas content. Desorption gas content was measured by the ISO-300 system under a temperature of 80 °C (Figure 2) when the sealed shale samples were placed in the desorption tank. Losing gas content was calculated by the United States Bureau of Mine (USBM) [12]. The samples (100–200 g) were placed in the residual gas tank, and then crushed for 30 min. Finally, residual gas content can be measured by the ISO-300 system (Figure 2).

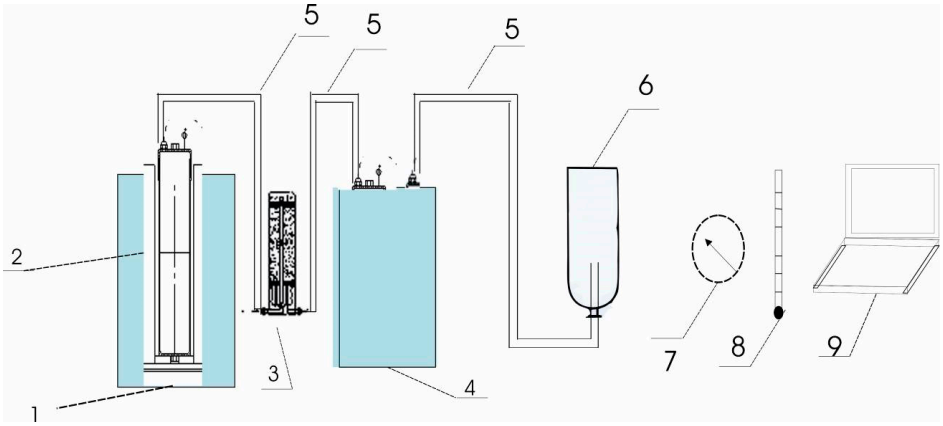

Figure 2. The ISO-300 filed testing system of desorption gas content in the Da'anzhai shale member.1-thermostatic apparatus; 2-desorption tank; 3-dehumidication apparatus; 4-testing instruments of gas flow; 5-flexible pipe; 6-device for collecting gas; 7-pressure gauge; 8-thermometer; 9-data-processing system.

4. Results and Discussions

4.1. Organic Geochemical Characteristics

According to the TOC determination and Rock-Eval data of 143 samples in wells FY3-2 and XL101, The TOC of the Da'anzhai member widely ranged from 0.05 wt.% to 3.08 wt.% (avg. 1.12%)

(Figure 3 and Table 1). Some 65% of samples have a TOC value of more than (>0.5 wt.%). The TOC level over 1.0 wt.% and 2.0 wt.% account for 45.1% and 8.9% of all samples, respectively. The variation of TOC value in vertical is related to lithology (Figure 3). The laminated calcareous shale and massive argillaceous shale in the upper part of the J_1zDa^2 have high TOC value of avg. 1.58 wt.% [13], while the massive or bedded marl and silty mudstone in the J_1zDa^1 and J_1zDa^3 have a low TOC of <0.50 wt.%. The potential yield (P), defined as the sum of Rock-Eval S1 and S2 values, is generally used to evaluate the genetic potential of a source rock [14]. P (S1+S2) and TOC are the most important indicators of organic matter abundance [15], and they show a good positive correlation (R^2 = 0.82) for all samples (Figure 3). P has a range of 1.03–6.84 mg/g (avg. 2.34 mg/g). The chloroform bitumen"A" content of 20 samples vary between 0.01% and 0.19% with an average value of 0.11% (Figure 3). Based on the thresholds of nonmarine source rocks from [15], the Da'anzhai member shale is a fair-good source rock and provides a good quality for hydrocarbon generation.

The kerogen composition analysis of 42 samples indicate all samples are dominated by sapropelinite (65–74%), along with moderate vitrinite (25–51.7%) (Figure 4). The sapropel organic matter is mostly correlated with initial production of algae or bacterial phytoplanktonic sources at the surface of lake [16]. The plot of HI vs. Tmax (Figure 4) indicates organic matter (OM) in the Da'anzhai member shale is dominated by type II, mainly typeII_2 [17]. The OM type in vertical transitioned from mainly typeII_2 in J_1zDa^3 to typeII_1 in the J_1zDa^2 and J_1zDa^1. This suggests the change of the OM origins in vertical result in the diversity of kerogen compositions and OM types.

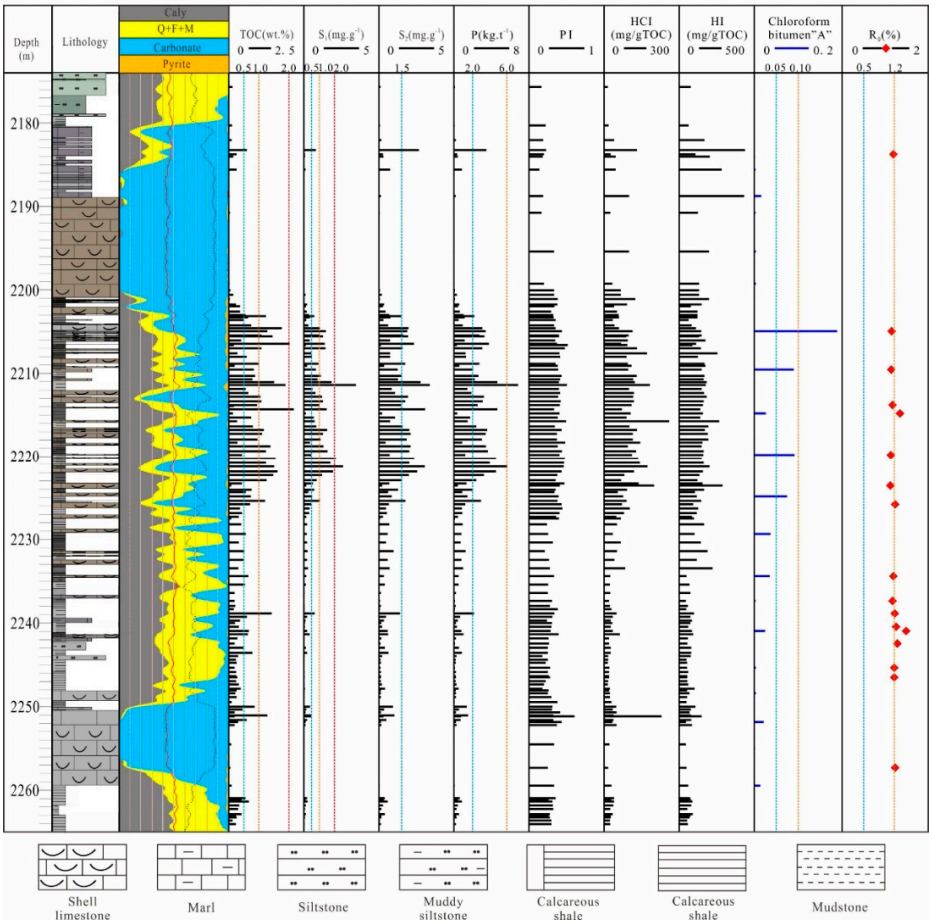

Figure 3. The geochemical and mineralogy characteristics for well FY3-2 in the Jurassic Da'anzhai member. Q: quartz; F: feldspar; M: mica. P = S_1+S_2; PI = S_1/(S_1+S_2); HCl = S_1/TOC × 100; HI = S_2/TOC × 100. The blue, orange, and red dash lines show the classification borders of general, good, and excellent qualities of source rock.

Table 1. The mineral composition and pore structure characteristics of shale samples.

Sample	TOC (wt.%)	Clay (wt.%)	Carbonate (wt.%)	Quartz (wt.%)	Pyrite (wt.%)	I/S (wt.%)	Illite (wt.%)	Kaolinite (wt.%)	Chlorite (wt.%)	Surface Area (m^2/g)	Pore Volume ($cm^3/100g$)	Porosity (%)	Permeability (mD)	Average Pore Size (nm)	Medium Pore Size (nm)
FY-1	0.56	8.7	75.6	7.4	1.6	2	3.04	1.83	1.83	1.76	1.09	0.8	0.103	62.50	41.7
FY-2	1.31	27.4	47.5	15.6	6.9	8.22	9.86	4.38	4.93	5.69	3.33	2.6	0.965	49.27	4.7
FY-3	1.89	22.7	55	15.7	3.8	6.13	6.81	5.22	4.54	3.80	2.55	2	0.097	49.80	36
FY-4	1.36	50.6	11.4	26.4	4.6	24.79	15.18	5.06	5.57	8.79	0.35	0.6	28.79	41.51	18
FY-5	0.81	9.5	79.5	6.8	2.7	2.57	3.61	1.52	1.81	2.19	2.09	1.6	0.083	80	22.5
FY-6	0.96	37.6	28.3	27	2.1	13.54	11.66	4.89	7.52	2.65	2.58	2	0.638	57.97	15.4
FY-7	1.23	22.8	54.8	15.8	2.2	6.384	9.58	3.88	2.96	3.36	2.72	2.1	0.961	170.21	102.3
FY-8	0.77	35.7	20.1	35.3	2.4	13.21	9.99	7.14	5.36	2.86	0.9	0.7	0.142	38.67	9.9
FY-9	1.21	50	19	24.5	1.4	15.5	15	10.5	9	3.71	4.44	3.5	9.79	35.00	7.2
FY-10	0.41	48.3	0	32.4	0	16.91	11.59	11.59	8.21	1.66	3.05	2.4	1.07	39.71	4.9
FY-11	0.33	12.7	76.1	11.2	0	3.18	2.54	3.05	3.94	1.42	2.16	1.7	0.565	31.06	9.7
FY-12	0.2	51.1	17.7	31.2	0	20.44	15.84	9.71	5.11	13.92	0.67	0.7	0.205	21.85	4.6
FY-13	0.61	46.3	10.3	40.5	0	19.45	15.28	6.95	4.63	12.62	1.12	0.9	0.073	17.78	4.2
FY-14	0.67	44.7	10.5	42.6	0	19.22	13.41	6.71	5.36	4.47	7.01	5.6	0.323	9	6.5
FY-15	0.49	45.3	18.6	32.2	1.8	19.48	16.31	5.44	4.08	9.47	4.7	5.9	9.02	163.73	100.9
FY-16	0.27	21.9	17.8	55.2	0	7.67	5.69	4.59	3.94	5.51	2.56	2	0.126	25	2.7
FY-17	0.26	48.3	18.6	31.4	0	18.84	14.97	9.66	4.83	11.91	2.25	1.7	0.154	27.44	4.5
FY-18	1.29	62.4	8.8	23.7	1.6	21.84	24.96	10.61	4.99	8.73	3.22	2.5	4.65	46.94	6.5

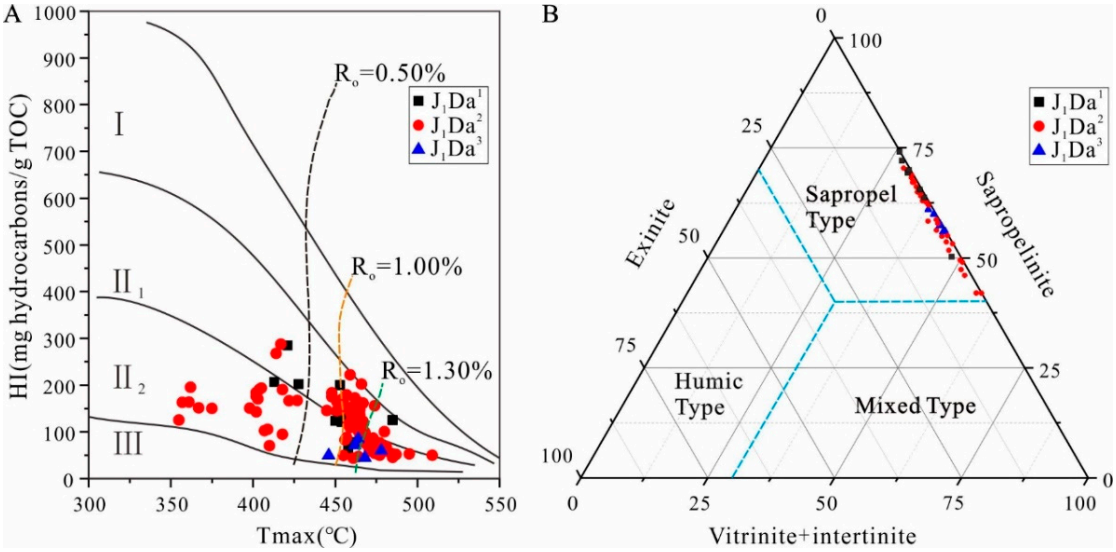

Figure 4. The organic matter type of Da'anzhai member shale. (**A**) Cross-plot between hydrogen index and Tmax showing the kerogen-type and source potential; (**B**) ternary chart of kerogen maceral composition.

The vitrinite reflectance (R_o) values of 17 samples ranged from 1.0% to 1.46% and averaged 1.19% (Figure 3). The temperature of maximum development of the S2 peak (T_{max}) mainly ranges from 439 °C to 510 °C (avg. 452 °C). This indicates most of the samples reach a moderate-high maturity with a high potential for shale gas generation [18].

4.2. Reservoir Characteristics

4.2.1. Mineral Composition and Reservoir Properties

X-ray diffraction analysis of core samples from the two wells showed that the Da'anzhai Member shale is dominated by carbonate minerals (avg. 56.8%), followed by clay minerals (avg. 29.8%), quartz and feldspars (avg. 19.6%), and pyrite (avg. 3.05%) (Figure 3 and Table 1). These kinds of mineral compositions confirmed that the Da'anzhai member shale is not a typical shale of mainly terrigenous origin (generally defined by clay contents greater than 75%). The brittle mineral content (avg. 68.5%) of the Da'anzhai member shale has reached at the minimum standards of fracturing feasibility (40%) [19]. Illite and mixed-layerillite/smectite (avg. 65.8%) are the predominant clay minerals from the corresponding clay mineral data (Table 1) with comparatively small amounts of chlorite (avg. 15.8%) and kaolinite (avg. 18.2%). According to the mineral compositions, sedimentary genesis, and structure, the lithofacies of the Da'anzhai member can be classified as five groups: marl (ML), calcareous shale (CS), argillaceous shale (AS), muddy siltstone (MS), and silty shale (SS).

Porosity and permeability analyses from MIP in well FY3-2 indicates that the differences of reservoir properties between several lithofacies are dramatic. There is a weakly positive relationship between Porosity and permeability (R^2 = 0.31) (Figure 5). The permeability of different lithofacies influenced by microfractures shows a wide range of 0.07–28.76 mD (Table 1). A permeability of 0.1–1 mD account for 66.7% in all samples. The permeability of CS with the laminated structures is relatively high. Moreover, its porosity (avg. 4.72%) is also higher than AS (avg. 2.72%), followed by MS (avg. 1.89%) and SS (avg. 1.75), whereas porosity of ML is relatively poor (avg. 1.02%). The information of pore throat size, the sorting and connectivity within pores also can be obtained from the MIP data and curves (Figure 6). The distribution of pore throat size indicates that AS, CS, and SS contains two types of pores: small pores (8–100 nm) and large pores (1–15 μm) with a good connectivity (Figure 7). But the tight ML and MS composed of a large number of small pores (<20 nm).

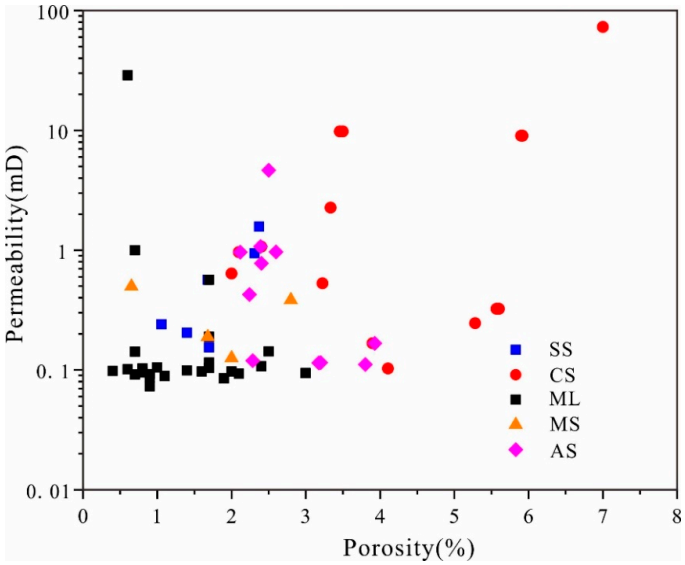

Figure 5. The relationship between porosity and permeability of 62 core samples. These samples were classified based on lithofacies. Note: SS: silty shale; CS: calcareous shale; ML: marl; AS: argillaceous shale; MS: muddy siltstone.

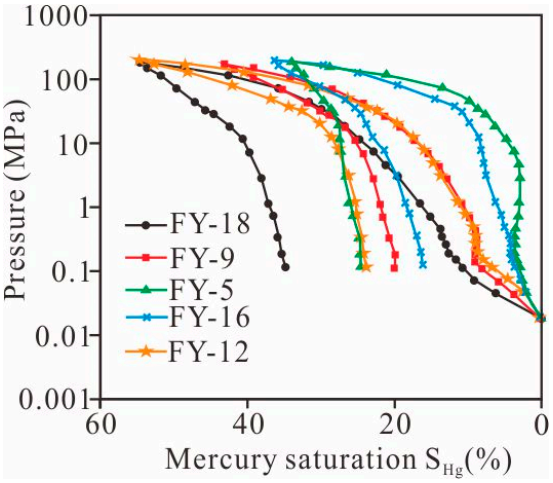

Figure 6. The capillary pressure curves of five typical types of lithofacies. Sample FY-5 of ML; sample FY-12 of SS; sample FY-9 of AS; sample FY-16 of MS; sample FY-9 of CS.

NMR is also an effective tool to determine the probe reservoir characteristics, including bound fluid, free fluid porosity, effective porosity, total porosity, and hydrocarbon existence [20]. The reservoir evaluation results of the Da'anzhai member from NMR well logging were shown in Figure 8 and Table 2. The heterogeneity of shale lithofacies strongly influenced the T_2 spectrum and porosity characteristics from NMR logging data. CS generally constitute of 2–3 peaks in the T_2 spectrum: The first peak (around 3 ms) is the largest peak, followed by a second peak (around 60 ms), while the third (1000 ms) peak is generally missing or it is not significant. This indicates that the pore types mainly consist of micropores and meso/macro pore. Sometimes, the fractures can be developed in these kinds of lithofacies. This is consistent with the distribution of pore throat size from the MIP results. The porosity of bound water is larger than that of free fluid. The T_2 spectrum of AS, SS, and MS shows an amplitude peak and a minor peak. However, the value of T_2 in the AS is generally higher than that of SS and MS. This indicates the AS has better reservoir quality. The T_2 spectrum of ML differs significantly from other lithofacies. It only has one peak around 1 ms, indicating that micropores prevail. Interestingly,

free water volume does not exist in the ML because of high carbonate cementation. This is further confirmed by the carbonate content from XRD results.

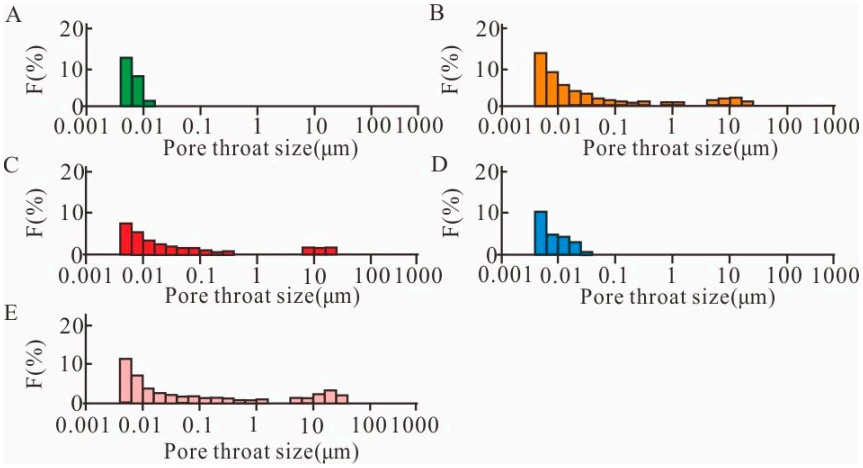

Figure 7. The distribution characteristics of pore throat size in five types of lithofacies. (**A**) for sample FY-5 of marl; (**B**) for sample FY-12 of silty shale; (**C**) for sample FY-9 of argillaceous shale; (**D**) for sample FY-16 of muddy siltstone; (**E**) for sample FY-9 of calcareous shale. F: Frequency.

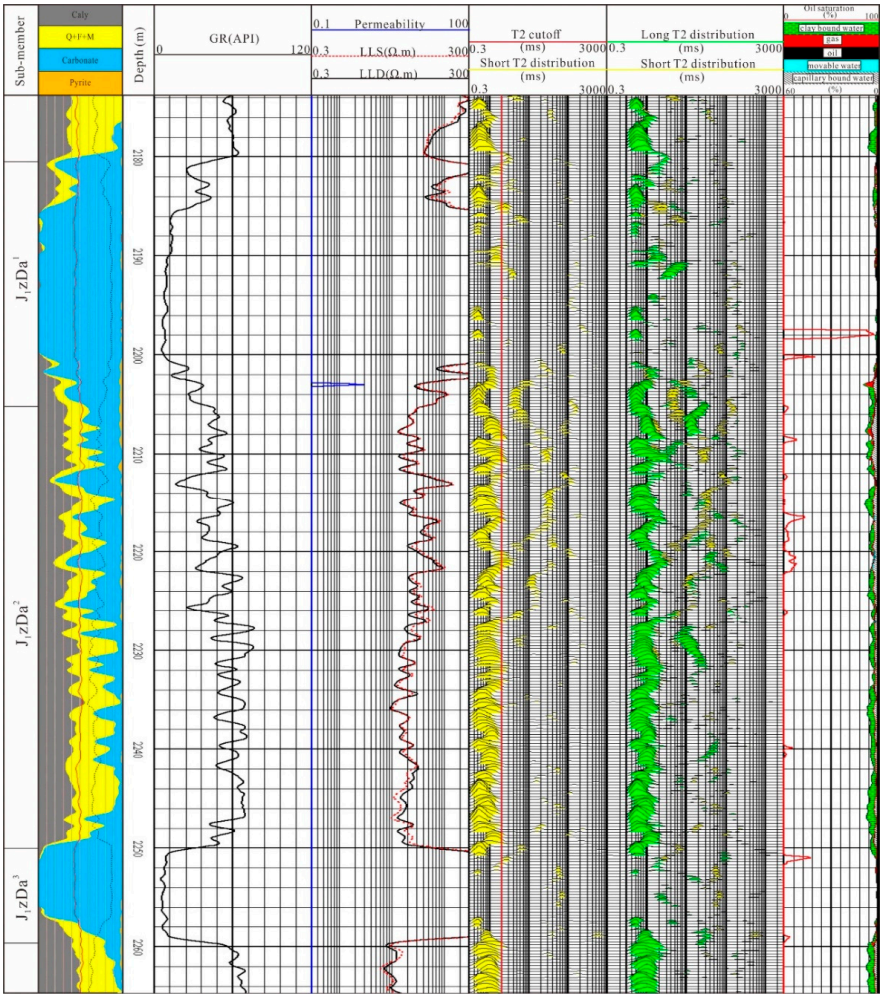

Figure 8. The reservoir evaluation from NMR logging data in the Da'anzhai member, well FY3-2.

Table 2. The reservoir evaluation results of five types of shale lithofacies in the Da'anzhai member from NMR well logging data.

Lithfacies Type	The Peak of T_2 Distribution (ms)	Capillary Bound Water Volume (avg. %)	Movable Water Volume (avg. %)	Effective Porosity (avg. %)	Total Porosity (avg. %)
CS	3–30, 60–300, 1000	2.3	0.6	2.5	4.9
AS	3–30, 30–100	1.5	0.4	1.8	2.1
SS	1–3 3–30	1.2	0.3	1.3	1.8
MS	0.3–3, 3–10	0.6	0.2	0.9	1.2
ML	0.3–3	0.3	0	0.5	0.9

4.2.2. Pore Morphology and Pore Structure Analysis

FE-SEM images are the techniques that are generally used to qualitatively determine the pore morphology characteristics of shales (e.g., the shapes, sizes, and distributions) [21–23]. The FE-SEM images show that a large quantity of micro-nano pores and microfracture exits may occur in the lacustrine shale samples. Based on the relationship between pores and minerals, pores can be classified into the three groups: organic matter-hosted pores (OM pores), the pores in the framework minerals (FM pores), and clay minerals-associated pores (CM pores). OM pores usually form during the thermal evolution and hydrocarbon generation process of kerogen and other OM. They mainly have aspherical, ellipsoidal-shape with a pore size of 2–100 nm (Figure 9A,B). Compared with the marine shale in the Fuling areas [5], OM pores are scarce in the Da'anzhai Lacustrine shale because of a moderate maturity (R_o: avg. 1.19%) and low TOC content. A large number of clay mineral pores was investigated in the SEM. The intrapartical and interlayer pores were developed between the clay mineral. The pore size of the observed wedge-shaped pore is 50 nm to 700 nm, and the length of the slits is up to 6 μm (Figure 9C,E,F). These pores provide a large surface for adsorbed gas. FM pores are mostly a certain amount of nano-scale pyrite framboids or calcite intercrystalline pores (Figure 9G,H). These pores are generally irregular with poor connectivity. The FM pores also contain the nano-scale pores generated by the dissolution of minerals (e.g., quartz and calcite) (Figure 9I). Moreover, a large number of microcracks could be investigated in the CS and AS. These shrinkage cracks were generally caused by dehydration of clay minerals and thermal pressurization of hydrocarbons [24,25], forming a crack-pore network system (Figure 9A,D). The shrinkage crack and the edge of the mineral particle form a bend-ridge-like distribution, with crack spacing of 20–30 nm and length of 8–40 μm. These microcracks provide important channels for gas migration.

Pore structure parameters measured by MIP are shown in Table 1. The average pore size and medium pore size show a main range of 17.8–57.9 nm and 2.7–18 nm, respectively. This indicates the pore size in the Da'anzhai member shale is dominated by mesopores, which is in consistent with the full pore-size distribution results of previous studies in Da'anzhai member shale of the central or northeastern Sichuan Basin [3–5]. The specific surface area varies from 1.42 to 13.92 m^2/g (avg. 5.81 m^2/g). The pore volume ranges from 0.35 to 7.01 $cm^3/100g$ (avg. 2.59 $cm^3/100g$). Compared with the marine Longmaxi Formation shale in the same area (i.e., Fuling area; [5]), the surface area and pore volume is much lower because a lower TOC of lacustrine shale in Da'anzhai member contributes less to the surface and pore volume than marine shale. In Figure 10, TOC values are positively correlated with surface area and pore volume with a coefficient of 0.46 and 0.23, respectively. However, this correlation is much poorer because of a low-medium TOC value (avg. 1.12 wt.%) and moderate maturity. The clay mineral and surface area exit a strong positive correlation with a coefficient of 0.62. This indicates clay mineral play a more important role on the surface area [26] and pore volume of lacustrine shale with a low TOC (Figure 10). Many interparticle pores among clay minerals are also investigated in the SEM (Figure 9C,E,F). On thecontrary, the carbonate content is negatively correlate with surface area and pore volume, because high carbonate minerals (e.g., calcite) with a strong cementation can greatly influence reservoir quality and usually have adverse impacts. The quartz minerals show a weakly positive relationship with pore volume (R^2 = 0.49). The total pore volume

increases with quartz and feldspar content in the lacustrine shale due to the generation of pores by dissolution and weakening of compaction [27].

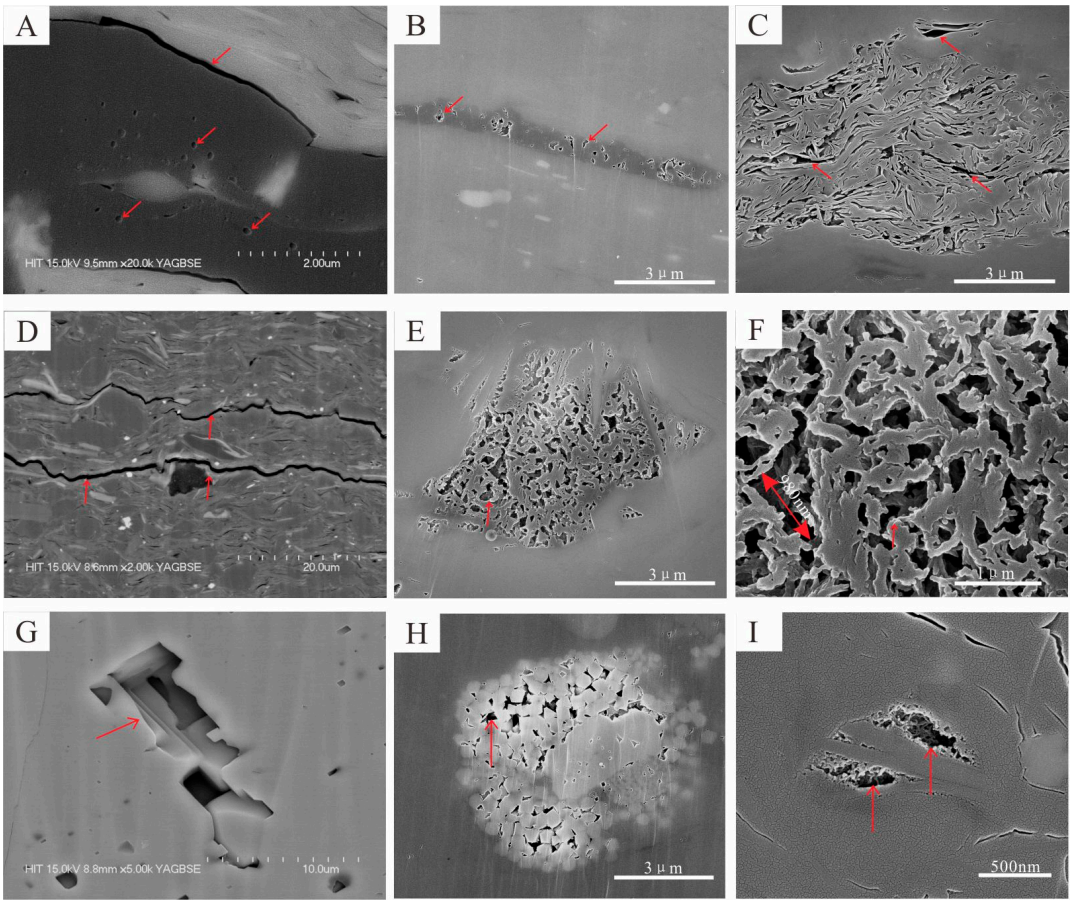

Figure 9. Pore types of the Da'anzhai member shale in the FE-SEM images. (**A**) organic matters-hosted pores and microfractures, CS, 2599.95 m, Well FY1; (**B**) organic matters-hosted pores, AS, 1736.51 m, well FY4; (**C**) interparticle pores between clay minerals, AS, 2543.73 m, well FY5; (**D**) microfractures, 2615 m, CS, well FY1; (**E**) and (**F**) floccule intercrystal pores in flocculated clay microfabric, CS, 2544.36 m, well FY4; (**G**) intercrystalline pores in calcite mineral, ML, 2639.8 m, well FY1; (**H**) intercrystal pores in pyrite framboids, SS, 1736.51 m, well FY4; (**I**) dissolution pores in calcite minerals, MS, 2672.04 m, well 5.

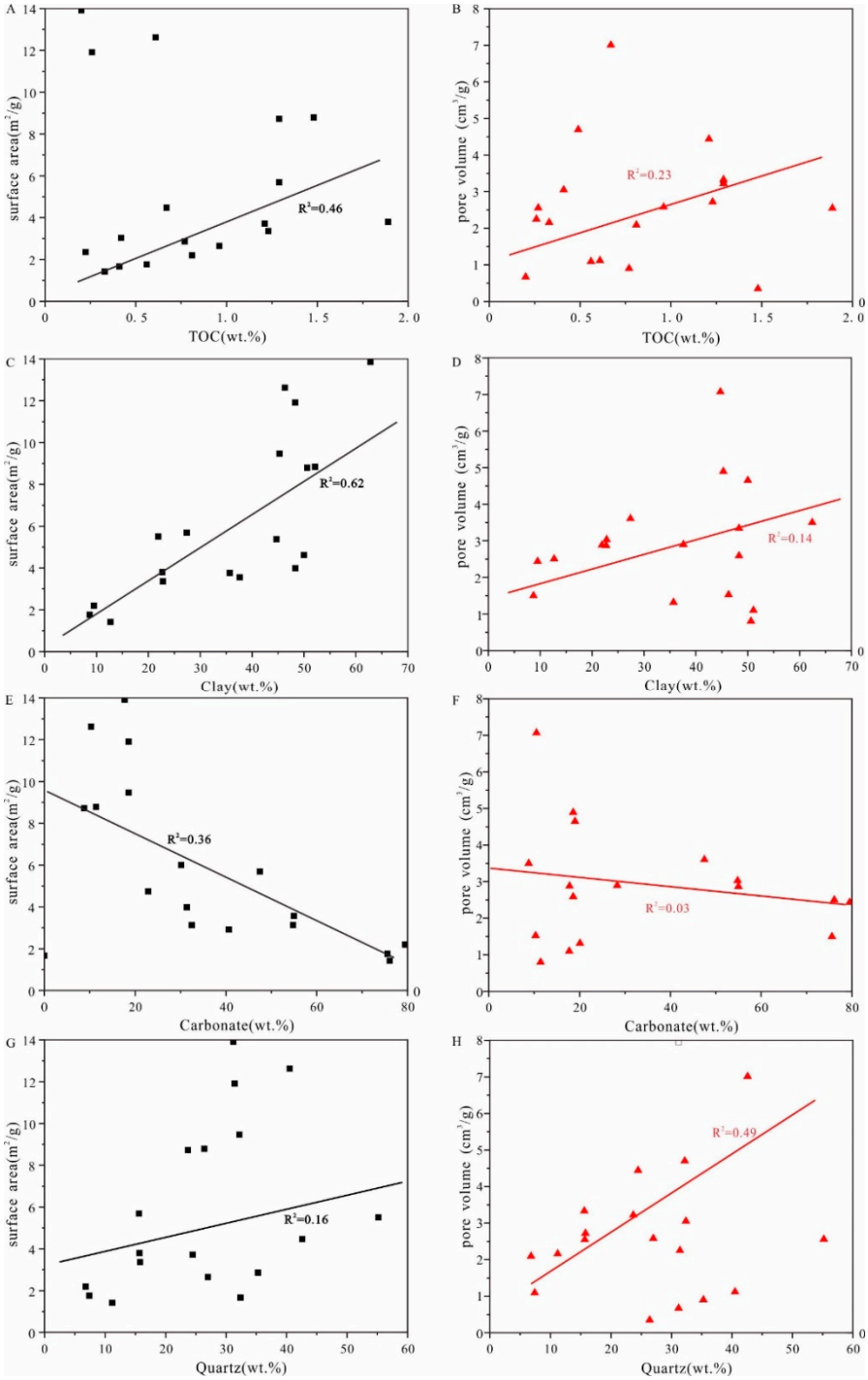

Figure 10. Correlation plots between specific surface area and pore volume and TOC and mineral composition. (**A**) The relationship between TOC and surface area; (**B**) The relationship between TOC and pore volume; (**C**) The relationship between clay and surface area; (**D**) The relationship between clay and pore volume; (**E**) The relationship between carbonate and surface area; (**F**) The relationship between carbonate and pore volume; (**G**) The relationship between Quartz and surface area; (**H**) The relationship between Quartz and pore volume.

4.3. Methane Sorption and Adsorption Potential

The methane adsorption isotherms of five shale samples measured at different pressure and temperatures are shown in Figure 11. We set a temperature group of 30 °C, 80 °C, 100 °C. The pressure

values were measured at the 13 balance pressure points. The balancing time at each spot was set by 12.0 h. The amount of methane adsorbed into the shale at early stage of <5 MPa rapidly increased under different temperature and reached 85% of the maximum adsorption capacity. However, the shale with a high TOC content at same temperature (80 °C) has much faster methane adsorption rate with a large gradient (Figure 11A), because a high TOC of organic-rich shale provide a large amount of surface area for methane adsorption. The increased amount of methane adsorption became less from 5 MPa up to 12 MPa, because the methane adsorption reached equilibrium state. This process can be described by the Langmuir isotherm equation [28]:

$$V = \frac{VLbp}{1 + bp} \tag{1}$$

where V is the absorbed methane volume, cm^3/g; V_L is the Langmuir volume, cm^3/g; b is the reciprocal of Langmuir pressure, MPa^{-1}; p is the pressure, MPa. Langmuir volume of Da'anzhai member shale ranges from 1.34 mL/g to 2.28 mL/G (avg. 1.70 mL/g), indicating medium-high adsorbed capacity (Table 3). However, shale with different TOC content has quite different V_L value at the same temperature (80 °C). When TOC content increased from 0.41 wt.% to 1.48 wt.%, the Langmuir volume of shale changed from 1.34 mL/g to 1.77 mL/g (Figure 11). Even with a similar TOC level, the Langmuir volume decreased rapidly at a high temperature. When the experimental temperature jumped from 30 °C to 100 °C, the Langmuir volume of shale decreased from 2.28 mL/g to 1.44 mL/g. This can be interpreted by adsorption potential theory.

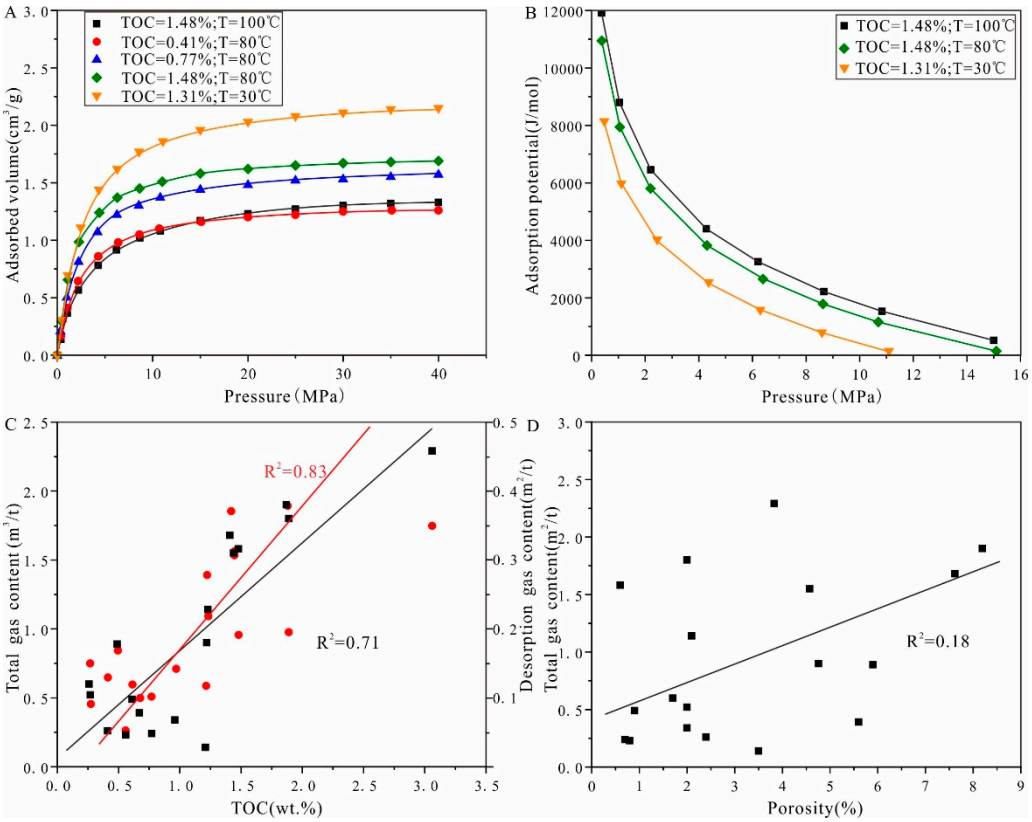

Figure 11. The gas potential of the Da'anzhai member shale. (**A**) and (**B**) isothermal adsorption curves and adsorption potential at different temperatures; (**C**) and (**D**) relationship between TOC, porosity and total gas content.

Table 3. Methane adsorption results and field desorption results of shale samples.

Sample	TOC (wt.%)	Porosity (%)	Langmuir Volume (mL/g)	Langmuir Pressure (MPa)	Desorption Gas Content (m^3/t)	Lost Gas Content (m^3/t)	Residual Gas Content (m^3/t)	Total Gas Content (m^3/t)
FY-1	0.56	0.8	/	/	0.04	0.19	0	0.23
FY-3	1.89	2.0	/	/	0.19	1.51	0.1	1.8
FY-4	1.48	0.6	1.77	2.01	0.19	1.27	0.12	1.58
FY-6	0.96	2.0	/	/	0.14	0.11	0.09	0.34
FY-7	1.31	2.1	2.28	2.46	0.22	0.85	0.07	1.14
FY-8	0.77	0.7	1.66	2.39	0.1	0.06	0.08	0.24
FY-9	1.21	3.5	/	/	0.11	0.02	0.01	0.14
FY-10	0.41	2.4	1.34	2.42	0.13	0.07	0.06	0.26
FY-13	0.61	0.9	/	/	0.12	0.32	0.05	0.49
FY-14	0.67	5.6	/	/	0.1	0.24	0.05	0.39
FY-15	0.49	5.9	/	/	0.17	0.66	0.06	0.89
FY-16	0.27	2.0	/	/	0.09	0.39	0.04	0.52
FY-17	0.26	1.7	/	/	0.15	0.45	0	0.6
XL-1	1.44	4.6	/	/	0.31	0.08	1.16	1.55
XL-2	1.87	8.2	/	/	0.38	0.15	1.37	1.9
XL-3	3.06	3.8	/	/	0.35	0.03	1.91	2.29
XL-4	1.41	7.6	/	/	0.38	0.06	1.24	1.68
XL-5	1.22	4.8	/	/	0.28	0.13	0.49	0.9

Note: /: no data.

Based on Polanyi's theory of adsorption potential [29], the adsorption potential correlated with pressure can be defined as:

$$\varepsilon = \int_{Pi}^{P0} \frac{RT}{P} dP = RT \ln \frac{P0}{Pi} \quad (2)$$

where ε is the adsorption potential, J/mol; P_i is the equilibrium pressure of methane at temperature T, MPa; P_0 is the saturated vapor pressure of methane at T, MPa; R is a constant value of 8.3114, J/(mol·K); T is the thermodynamic temperature, K; P is the pressure, MPa; under a certain temperature, the saturated vapor pressure of methane keeps constant. For example, the saturated vapor pressure of methane is generally 15.8 MPa at 80 °C. So according to Equation (2), the adsorption potential of shale samples can be easily determined from isothermal adsorption experiment (Figure 11B). When the temperature increased under the same pressure, the adsorption potential obviously increased. It indicates the result of an increase of temperature and gas molecular kinetic energy. The increase of adsorption capacity cannot keep more gas molecules absorbed by the adsorbent, because the increasing rate of energy change is much lower than the kinetic energy. Therefore, the adsorption capacity increases with the decrease of temperature.

4.4. Gas Content of Field Desorption

Field desorption analysis of 18 samples indicates total gas content of the Da'anzhai member shale range from 0.14 to 2.29 m^3/t (avg. 1.04 m^3/t). It is much greater than the minimum standard of 0.5 m^3/t for a favorable lacustrine shale gas [2]. Moreover, the CES in the medium-upper section of the J_1zDa^2 has high gas content with a range of 1.15–2.29 m^3/t (avg. 1.57 m^3/t). Desorption gas content accounts for 10.56–60.44% (avg. 26.75%) of total gas content. This is much lower than the ratio of desorption gas content to total gas content due to a moderate TOC and maturity. TOC is positively related to the total gas content with a correlation coefficient of 0.71 (Figure 11C). It shows a strongly positive relationship between TOC and desorption gas content (R^2 = 0.83). This suggests OM contributes most to desorption gas content. There is also a weakly positive correlation between porosity and total gas content (Figure 11D), because shale with a high porosity can provide more sites for free gas.

5. Conclusions

(1) The lacustrine Da'anzhai member shale in the north Fuling area has a medium-high OM content (avg. TOC 1.12 wt.%). The laminated calcareous shale in the upper part of the J_1zDa^2 has high TOC value of avg. 1.58 wt.%. The average potential yield P (S1 + S2) and chloroform bitumen content "A" are 2.34 mg hydrocarbons per g TOC and 0.11% with a medium hydrogen generation potential. The kerogen type of mainly typeII_2 and a moderate OM maturity (VR = avg. 1.19) indicate a huge potential of gas generation. The mineral content is dominated by calcite, clay and quartz. The clay minerals mainly consist of illite and mixed-layerillite/smectite. The lithofacies of the Da'anzhai member includes marl (ML), calcareous shale (CS), argillaceous shale (AS), muddy siltstone (MS), and silty shale (SS).

(2) Heterogeneity of shale lithofacies strongly influences the reservoir quality. The porosity and permeability of shale is overall low, but the laminated calcareous shale has good reservoir properties with a high porosity (avg. 4.72%). The pore size is dominated by mesopores, and the medium pore diameter is 23.2 nm. Better NMR data show that the small pores with the transverse relaxation time of 0.6–1 ms and 1–3 ms comprised most of the porosity of the Da'anzhai shale member, while the larger pores with a T_2 value of 300–1000 ms and 1000–3000 ms only accounts for a small porosity proportion. However, it is very important for gas migration and generally showed a third peak in the NMR spectrum of CS, and this peak generally missed after centrifuge processing.

(3) The clay minerals in Da'anzhai member shale contributes most to surface area. The average Langmuir volume and total gas content is 1.7 mL/g and 1.04 m^3/t. The adsorption capacity of methane decreases with decreasing TOC and increasing temperature. The total gas content of lacustrine shale is controlled by TOC and porosity. CS have the highest gas content (avg. 1.57 m^3/t) than other shale lithofacies. The reservoir properties, mineral composition and gas content data suggest the laminated calcareous shale in the medium-upper section of the J_1zDa^2 are the most advantage lithofacies for shale gas potential production.

Author Contributions: Conceptualization, J.H. and H.D.; investigation, J.H., H.D., R.M., R.W.; methodology, J.H., H.D.; formal analysis, J.H., R.W., A.L.; resource, H.D., J.H.; data curation, J.H., R.M., Y.W.; Writing—Original draft preparation, J.H.; writing—Review and editing, J.H., H.D., Y.W.; visualization, J.H.; project administration, D.H., R.W.; funding acquisition, J.H., R.W. All authors have read and agreed to the published version of the manuscript.

Funding: This research was supported by supported by State Key Laboratory of Shale Oil and Gas Enrichment Mechanisms and Effective Development (G5800-19-ZS-KFGY006).

Conflicts of Interest: The authors declare no conflict of interest.

References

1. Wei, X.F.; Huang, J.; Li, Y.P.; Wang, Q.B.; Liu, R.B.; Wen, Z.D. The main factors controlling the enrichment and high production of Da'anzhai member continental shale gas in Yuanba area. *Geolog. China* **2014**, *41*, 970–981.
2. Nie, H.K.; He, Z.L.; Liu, G.X.; Zhang, G.R.; Lu, Z.Y.; Li, D.H.; Sun, C.X. Status and direction of shale gas exploration and development in China. *J. China Univ. Mining Technol.* **2020**, *49*, 13–35.
3. Xu, Q.L.; Liu, B.; Ma, Y.S.; Song, X.; Wang, Y.; Chen, Z. Geological and geochemical characterization of lacustrine shale: A case study of the Jurassic Da'anzhai member shale in the central Sichuan Basin, southwest China. *J. Nat. Gas. Sci. Eng.* **2017**, *47*, 124–139. [CrossRef]
4. Long, L.Y.; Zhang, Y.Z.; Wang, Y.J.; Wang, L.G. The pore structure of tight limestone-Jurassic Ziliujing Formation, Central Sichuan Basin, China. *App. Geophys.* **2018**, *15*, 165–174.
5. Chen, L.; Jiang, Z.X.; Liu, Q.X.; Jiang, S.; Liu, K.; Tan, J.; Gao, F. Mechanism od shale gas occurrence: Insights from comparative study on pore structures of marine and lacustrine shales. *Mar. Pet. Geol.* **2019**, *104*, 200–216. [CrossRef]
6. Xu, H.; Zhou, W.; Hu, Q.H.; Xia, X.H.; Zhang, C.; Zhang, H.T. Fluid distribution and gas adsorption behaviors in over-mature shales in southern China. *Mar. Pet. Geol.* **2019**, *109*, 223–232. [CrossRef]

7. Zhai, G. *Petroleum Geology of China*; Petroleum Industry Press: Beijing, China, 1997.
8. Gao, J.; Wang, X.; He, S.; Guo, X.; Zhang, B.; Chen, X. Geochemical characteristics and source correlation of natural gas in Jurassic shales in the North Fuling area, Eastern Sichuan Basin, China. *J. Pet. Sci. Eng.* **2017**, *158*, 284–292. [CrossRef]
9. Coates, G.R.; Xiao, L.; Prammer, M.G. *Nmr Logging: Principles and Applications*; Haliburton Energy Services: Houston, TX, USA, 1999.
10. Neto, A.C.; Guinea, F.; Peres, N.M.; Novoselov, K.S.; Geim, A.K. The electronic properties of graphene. *Rev. Mod. Phys.* **2009**, *81*, 109. [CrossRef]
11. Testamanti, M.N.; Rezaee, R. Determination of Nmr T_2 cut-off for clay bound water in shales: A case study of Carynginia Formation, Perth Basin, Western Australia. *J. Pet. Sci. Eng.* **2017**, *149*, 497–503. [CrossRef]
12. Yao, G.H.; Wang, X.Q.; Du, H.Y.; Yi, W.; Guo, M.; Xiang, R.; Li, Z. Applicability of USBM method in the test on shale gas content. *Acta Pet. Sin.* **2016**, *37*, 802–806.
13. Milad, B.; Slatt, R. Outcrop subsurface reservoir characterization of the Mississippian Sycamore/Meramec play in the SCOOP area, Arbuckle mountains, Oklahoma, USA. In Proceedings of the Unconventional Resource Technology Conference, Denver, CO, USA, 22–24 July 2019.
14. Tissot, B.P.; Welte, D.H. *Petroleum Formation and Occurrence*, 2nd ed.; Springer-Verlag: Heidelberg/Berlin, Germany, 1984; p. 699.
15. Huang, D.F.; Li, J.C.; Zhang, D.J. *Evolution and Hydrocarbon Generation Mechanisms of Terrestrial Organic Matter*; Petroleum Industry Press: Beijing, China, 1984; pp. 1–228.
16. Schnyder, J.; Dejax, J.; Keppens, E.; Tu, T.T.N.; Spagna, P.; Boulila, S.; Galbrun, B.; Riboulleau, A.; Tshibangu, J.P.; Yans, J. An Early Cretaceous lacustrine record: Organic matter and organic carbon isotopes at Bernissart (Mons Basin, Belgium). *Palaeogeogr. Palaeoclimatol. Palaeoecol.* **2009**, *281*, 79–91. [CrossRef]
17. Taylor, G.H.; Teichmüller, M.; Davis, A.; Diessel, C.F.K.; Littke, R.; Robert, P. *Organic Petrology*; Schweitzerbart: Stuttgart, Germany, 1998; pp. 1–704.
18. Xu, H.; Zhou, W.; Zhang, R.; Liu, S.M.; Zhou, Q.M. Characterizations of pore, mineral and petrographic properties of marine shale using multiple techniques and their implications on gas storage capability for Sichuan longmaxi gas shale field in China. *Fuel* **2019**, *241*, 360–371. [CrossRef]
19. Rickman, R.; Mullen, M.J.; Petre, J.E.; Grieser, W.V.; Kundert, D. *A Practical Use of Shale Petrophysics for Stimulation Design Optimization: All Shale Plays Are Not Clones of the Barnett Shale*; Society of Petroleum Engineers: Denver, CO, USA, 2008.
20. Kapur, G.; Findeisen, M.; Berger, S. Analysis of hydrocarbon mixtures by diffusion-ordered Nmr spectroscopy. *Fuel* **2000**, *79*, 1347–1351. [CrossRef]
21. Loucks, R.G.; Reed, R.M.; Ruppel, S.C.; Hammes, U. Spectrum of pore types and networks in mudrocks and a descriptive classification for matrix-related mudrock pores. *AAPG Bull.* **2012**, *96*, 1071–1098. [CrossRef]
22. Tian, H.; Pan, L.; Xiao, X.M.; Wilkins, R.W.T.; Meng, Z.P.; Huang, B.J. A preliminary study on the pore characterization of Lower Silurian black shales in the Chuandong Thrust Fold Belt, southwestern China using low pressure N2 adsorption and FE-SEM methods. *Mar. Pet. Geol.* **2013**, *48*, 8–19. [CrossRef]
23. Milad, B.; Slatt, R.; Fuge, Z. Lithology, stratigraphy, chemostratigraphy, and depositional environment of the Mississippian Sycamore rock in the SCOOP and STACK area, Oklahoma, USA: Field, lab, and machine learning studies on outcrops and subsurface wells. *Mar. Pet. Geol.* **2020**, *115*, 1–18. [CrossRef]
24. Jarvie, D.M.; Hill, R.J.; Ruble, T.E.; Pollastro, R.M. Unconventional shale-gas systems: The Mississippian Barnett Shale of north-central Texas as one model for thermogenic shale-gas assessment. *AAPG Bull.* **2007**, *91*, 475–499. [CrossRef]
25. Ross, D.J.K.; Bustin, R.M. The importance of shale composition and pore structure upon gas storage potential of shale gas reservoirs. *Mar. Petrol. Geol.* **2009**, *26*, 916–927. [CrossRef]
26. Ji, L.; Zhang, T.; Milliken, K.L.; Qu, J.; Zhang, X. Experimental investigation of main controls to methane adsorption in clay-rich rocks. *Appl. Geochem.* **2012**, *27*, 2533–2545. [CrossRef]
27. Wang, Y.; Liu, L.F.; Li, S.T.; Ji, H.T.; Xu, Z.J.; Luo, Z.H.; Xu, T.; Li, L.Z. The forming mechanism and process of tight oil sand reservoirs: A case study of Chang 8 oil layers of the Upper Triassic Yanchang Formation in the western Jiyuan area of the Ordos Basin, China. *J. Pet. Sci. Eng.* **2017**, *158*, 29–46. [CrossRef]

28. Langmuir, I. The adsorption of gases on plane surfaces of glass, mica and platinum. *J. Am. Chem. Soc.* **1918**, *143*, 1361–1403. [CrossRef]
29. Polanyi, M. The potential theory of adsorption. *Science* **1963**, *141*, 1010–1013. [CrossRef] [PubMed]